Responses of Model Cortical Neurons to Temporal Interference Stimulation and Related Transcranial Alternating Current Stimulation Modalities

Boshuo Wang[a], Aman S. Aberra[b,1], Warren M. Grill[b,c,d,e], Angel V. Peterchev[a,b,c,e,*]

[a] Department of Psychiatry and Behavioral Sciences, School of Medicine, Duke University, Durham, NC 27710, USA

[b] Department of Biomedical Engineering, School of Engineering, Duke University, Durham, NC 27708, USA

[c] Department of Electrical and Computer Engineering, School of Engineering, Duke University, Durham, NC 27708, USA

[d] Department of Neurobiology, School of Medicine, Duke University, Durham, NC 27710, USA

[e] Department of Neurosurgery, School of Medicine, Duke University, Durham, NC 27710, USA

[1] A. S. Aberra is currently with the Department of Biological Sciences, Dartmouth College, Hanover, NH 03755, USA.

Email addresses:

boshuo.wang@duke.edu, aman.aberra@duke.edu, warren.grill@duke.edu, and angel.peterchev@duke.edu

[*] Corresponding author: A.V. Peterchev

Phone: +1 919 684 0383

E-mail: angel.peterchev@duke.edu

Address: Division of Brain Stimulation and Neurophysiology, Department of Psychiatry and Behavioral Sciences, Duke University, Box 3620, DUMC, Durham, NC 27710, USA

A preliminary version of this work was deposited in bioRxiv on May 4, 2022 (DOI: 10.1101/2022.05.04.490540). Preliminary results of this study were presented at the 1st and 2nd Carolina Neuromodulation Conference (May 2018 and June 2019, Chapel Hill, NC, USA), the 43rd Neural Interface Conference (June 2018, Minneapolis, MN, USA), Neural Interfaces 2021: The NANS-NIC Joint Meeting (June 2021, online), and the 4th International Brain Stimulation Meeting (Wang et al., 2021a) (December, 2021, Charleston, SC, USA).

Abstract

Background: Temporal interference stimulation (TIS) has been proposed as a non-invasive, focal, and steerable deep brain stimulation method. However, the mechanisms underlying experimentally observed TIS effects are unknown, and prior simulation studies have limitations in the representations of the TIS electric field (E-field) and cerebral neurons. **Objective:** To examine the E-field and neural response characteristics for TIS and other transcranial alternating current stimulation modalities. **Methods:** We simulated a range of stimulation parameters in layer 5 pyramidal neurons, including different orientations, frequencies, amplitude ratios, amplitude modulation, and phase difference of the E-fields, and obtained thresholds for both activation and block. **Results:** At the target region in the cortex, where the two E-fields have similar amplitudes, TIS generates an amplitude-modulated total E-field. The TIS E-field also exhibits rotation where the E-field orientations are not aligned, which generally co-localizes with the target. TIS activation thresholds are similar to high-frequency stimulation with or without modulation and/or rotation (75–230 V/m). Outside the target region, the TIS E-field is dominated by the high-frequency carrier, with minimal amplitude modulation and/or rotation, and it is less effective at activation and more effective at block. Unlike amplitude-modulated high-frequency stimulation, TIS creates block for some combinations of E-field orientations and amplitude ratios at very high amplitudes (>1700 V/m). **Conclusion:** TIS mechanisms may involve neural activity block and periodic activation or onset response, which occur at E-field strengths too high to be delivered tolerably through scalp electrodes and which may inhibit endogenous activity in off-target regions, suggesting limited significance of TIS.

Keywords: temporal interference stimulation, transcranial alternating current stimulation, kilohertz stimulation, computational simulation, neuron model

Funding: Research reported in this publication was supported by the National Institutes of Health of the United States of America under grants No. R01NS088674 and No. R01NS117405. The content is solely the responsibility of the authors and does not necessarily represent the official views of the funding agencies.

Introduction

Transcranial electric or magnetic stimulation can modulate the activity of neurons in the brain non-invasively to treat neurological and psychiatric disorders (Eldaief et al., 2013; Lefaucheur et al., 2014; Rossi et al., 2020; Reato et al., 2013; Caumo et al., 2012; Becker et al., 2019). Compared to invasive methods, the electric field (E-field) distribution of transcranial stimulation is more diffuse and shallow due to the large distance between the stimulation sources and the brain. For transcranial electrical stimulation (TES), the typical cortical area activated or exposed to significant E-field strength (e.g., more than half the maximum E-field) is on the order of square centimeters (Huang et al., 2017; Miranda et al., 2013). For magnetic stimulation (TMS), the fundamental depth-focality trade-off shows that activation of deep targets would result in widespread activation of more superficial brain regions (Deng et al., 2013; Gomez et al., 2018). Efforts to improve the spatial characteristics such as focality and depths of conventional stimulation methods mostly rely on improved geometric design of the stimulation devices: electrode montages (Datta et al., 2009; Dmochowski et al., 2011; Edwards et al., 2013; Huang and Parra, 2019) or coil designs (Gomez et al., 2018).

Methods that use the temporal domain and intrinsic neuronal properties have been proposed as a means to achieve more focal and/or deep transcranial electrical (Grossman et al., 2017; Vöröslakos et al., 2018) or magnetic (Sorkhabi et al., 2020) stimulation. These methods use multiple stimulation channels, e.g., comprised of separate pairs of scalp electrodes, to generate individual E-fields in the head with different temporal waveforms. Temporal interference stimulation (TIS), also referred to as interferential current therapy and applied as a neuromuscular treatment between the 1960s and 1990s (Goats, 1990; Kloth, 1987), was proposed for non-invasive brain stimulation (Grossman et al., 2017). In TIS, two high frequency (> 1 kHz) sinusoidal E-fields are applied with a slight frequency difference to create an amplitude-modulated (AM) total E-field through temporal interference. Borrowing terminology from radio technology, neurons are hypothesized to demodulate the low frequency (< 100 Hz) amplitude envelope of the summed E-field waveform via membrane current rectification due to the nonlinear properties of ion channels. Under this assumption, activation would occur mostly in deeper brain regions where the E-field amplitudes of the stimulation channels are similar and therefore the modulation depth (i.e., extent of

amplitude change due to the modulation) of the total E-field waveform is large. On the other hand, superficial brain areas would be unaffected, as the mismatch in E-field amplitudes generates negligible low frequency envelope, and neurons are thought to be insensitive to the large amplitude kHz carrier wave. Without repositioning the electrodes, TIS could steer the site of stimulation by adjusting the relative amplitudes of each channel to shift the region where the E-fields generate the largest amplitude and/or modulation depth of interference.

Grossman et al. (2017) reported experimental neuronal responses to TIS in the anesthetized mouse brain with current amplitude 2–5 times higher than the threshold for low frequency transcranial alternating current stimulation (tACS), whereas high frequency (kHz) tACS could not evoke responses even at seven times higher current amplitudes. However, the mechanism underlying these effects and its applicability to transcranial stimulation in humans remains unclear. One interpretation is that unmodulated kHz tACS does not significantly affect neurons, putatively due to low-pass filtering at the neuronal membrane, whereas the amplitude modulation exhibited by the summated TIS E-field generates low frequency neuronal membrane potentials that periodically activate the neurons. This explanation, however, does not take into account the fact that kHz stimulation can result in transient or sustained firing and, at higher stimulus amplitudes, neuronal activity block (Kilgore and Bhadra, 2004; Miles et al., 2007; Mirzakhalili et al., 2020; Pelot et al., 2017). These types of responses to kHz stimulation cannot be ignored given that the unmodulated kHz E-field has stronger absolute amplitude than the low frequency modulation envelope, and that the neuronal membrane can respond to kHz stimuli since experimentally measured time constants of the cortical response to transcranial stimulation are around 150–250 μs (Barker et al., 1991; D'Ostilio et al., 2016; Peterchev et al., 2013). Moreover, because the neuronal membrane should low-pass filter modulated and unmodulated kHz waveforms to a similar degree, membrane filtering would not favor the modulated E-field (Dmochowski and Bikson, 2017; Mirzakhalili et al., 2020). Thus, even if the effects of the unmodulated kHz stimulus were not detected with specific measurements, this does not necessarily mean that neurons were not impacted significantly. It is possible, for example, that kHz neuronal block suppress neural responses in regions away from the target (Mirzakhalili et al., 2020). In this case, focality of activation could be achieved, but endogenous brain activity in non-target regions may be adversely affected.

Various recent studies have aimed to explore the mechanisms of TIS, but have limitations in their methods and ability to distinguish between the competing mechanistic explanations outlined above. For example, the Grossman et al. (2017) study was in anesthetized mice, and while TIS did not appear to activate off-target brain regions, it is unclear whether it blocked or disrupted endogenous brain activity outside the target. Computational studies of suprathreshold TIS have focused on activation of isolated axons (fibers of passage) (Gomez-Tames et al., 2021; Howell and McIntyre, 2020; Mirzakhalili et al., 2020), which do not fully capture effects on cortical neurons. Moreover, the combination of the two TIS current waveforms results is a three-dimensional (3D) time-varying E-field distribution that can interact in complex ways with the 3D morphology of cortical neurons (Aberra et al., 2020), but the TIS E-fields and their effect on neurons have only been analyzed in one dimension (1D), either along the direction of largest modulation depth or in a predetermined direction such as the radial direction of the gray matter or along fiber bundles in the white matter (Esmaeilpour et al., 2021; Gomez-Tames et al., 2021; Grossman et al., 2017; Howell and McIntyre, 2020; Huang and Parra, 2019; Lee et al., 2020, 2022; Mirzakhalili et al., 2020; Rampersad et al., 2019; Song et al., 2021).

Translation of TIS from animal studies to clinical applications poses further challenges. With the same current amplitude, E-fields achievable in the human brain are two orders-of-magnitude smaller than those in mice due to differences in head size and cortical geometry. Conventional tACS currents delivered via scalp electrodes are limited to a few milliamps to be tolerable without anesthesia, generating subthreshold E-fields on the order of only 0.1 to 1 V/m throughout the human brain (Alekseichuk et al., 2019b; Huang and Parra, 2019; Louviot et al., 2022; Rampersad et al., 2019). Suprathreshold TIS in humans would therefore require much higher current amplitudes. Hence, estimation of the TIS E-field thresholds would provide key information for determining the clinical applicability of TIS.

To understand the biophysics underlying TIS, we analyzed the spatiotemporal characteristics of the TIS E-field and simulated the response of individual cortical neurons to TIS and several related tACS modalities. The TIS E-field exhibits some unique properties that may impact neural activation and are not reproduced with AM-tACS. However, the simulations show that block of ongoing off-target activity may occur and all mechanisms that can

account for the periodic neural activation by TIS require field strengths that are unlikely to be feasible in humans due to the high currents that need to be applied to the scalp.

Methods

Characteristics of TIS E-field

Unlike conventional tACS, the E-field of TIS consists of two or more spatial components that have different temporal characteristic. Whereas the E-field of each channel is considered quasi-static, and thus separable into spatial and temporal components (Bossetti et al., 2008; Plonsey and Heppner, 1967), the total TIS E-field is not. Each channels' E-field can be described as $\boldsymbol{E}_n = \boldsymbol{S}_n(\boldsymbol{s}) \cdot T_n(t)$, where $\boldsymbol{s}$ is the macroscopic spatial coordinate vector within the brain, t is time, and $n = 1,2 \ldots$ is the channel number. For simplicity, the temporal functions of the tACS channels are normalized: $T_n(t) = \sin(\omega_n t + \alpha_n)$, where ω_n and α_n are their frequency and initial phase. The E-field amplitudes are given according to their spatial distributions $|\boldsymbol{S}_n|$. Specifically for transcranial stimulation, the quasi-uniform approximation of the E-field on the microscopic scale of individual neurons (Bikson et al., 2013) is considered so that $\boldsymbol{S}_n$ is constant for individual neurons but varies depending on a neuron's cortical location (Aberra et al., 2018).

Aligned E-fields

With $\omega_1 \neq \omega_2$, a 1D AM interferential waveform only exists where the two local E-fields are aligned or anti-aligned (Figure 1A, top):

$$|\boldsymbol{E}_{\mathrm{TIS}}| = A_{\mathrm{TIS}}(t) \cdot \sin\big(\alpha_{\mathrm{TIS}}(t)\big) \quad .$$

where A_{TIS} and α_{TIS} are the envelope and instantaneous phase of the oscillation. The envelope

$$A_{\mathrm{TIS}}(t) = \sqrt{A_1^2 + A_2^2 + 2A_1A_2\cos(\Delta\omega t + \Delta\alpha)}$$

has a frequency of $\Delta\omega = \omega_2 - \omega_1$ and maximum and minimum amplitude of $A_1 + A_2$ and $|A_1 - A_2|$, in which the individual field amplitudes are $A_{1,2} = |\boldsymbol{S}_{1,2}|$ and the initial phase difference $\Delta\alpha = \alpha_2 - \alpha_1$ is typically 0° or 180° for TIS (aligned and anti-aligned, respectively). The instantaneous phase is

$$\alpha_{\mathrm{TIS}}(t) = \omega_1 t + \alpha_1 + \arctan\frac{A_2\sin(\Delta\omega t + \Delta\alpha)}{A_1 + A_2\cos(\Delta\omega t + \Delta\alpha)} \quad .$$

The TIS waveform's carrier frequency

$$\omega_{\mathrm{TIS}}(t) = \frac{\mathrm{d}\alpha_{\mathrm{TIS}}}{\mathrm{d}t} = \frac{A_1^2\omega_1 + A_2^2\omega_2 + A_1A_2(\omega_1+\omega_2)\cos(\Delta\omega t + \Delta\alpha)}{A_1^2 + A_2^2 + 2A_1A_2\cos(\Delta\omega t + \Delta\alpha)}$$

is constant and equals the mean of the two high frequencies only for equal amplitudes. For $A_1 \neq A_2$, however, ω_{TIS} has a low frequency jitter around the frequency of the channel with the larger amplitude (Figure 1A, bottom):

$$\bar{\omega}_{\mathrm{TIS}} = \frac{\omega_1+\omega_2}{2} + \frac{\Delta\omega}{2}\mathrm{sgn}(A_2 - A_1) = \begin{cases} \omega_1 & A_1 > A_2 \\ \dfrac{\omega_1+\omega_2}{2} & A_1 = A_2 \\ \omega_2 & A_1 < A_2 \end{cases} .$$

Due to the frequency's dependency on the amplitude ratio, the high frequency oscillations of the total E-field at different cortical locations have different phase shifts throughout their common low frequency period (Figure 1A, top), potentially resulting in asynchronous neural activation. This is similar to the traveling wave observed for two-channel tACS with the same frequency but a non-zero phase difference (Alekseichuk et al., 2019a).

Non-aligned E-fields

For non-aligned E-fields, the total E-field must be considered in 3D. In the plane spanned by the two E-field vectors, the total E-field traces out a dense Lissajous curve bounded by a parallelogram determined by the amplitude, orientation, and phase of the two E-fields (Figure 1B). For E-fields with similar amplitude and large angle (e.g., between 60° and 120°) between them, the total E-field alternates between oscillations and rotations at low frequency. The oscillation and rotation correspond to periods in time when the two E-fields are in-phase and out-of-phase and can be characterized by the ratio of the minimum and maximum E-field amplitude during one high frequency cycle.

The rotation of the E-field could be contributing to TIS stimulation. For example, rotational field TMS, applied using two perpendicular figure-of-eight TMS coils driven with the same current waveforms with a 90° phase shift, demonstrated lower thresholds and stronger evoked responses (Rotem et al., 2014; Roth et al., 2019, 2020). The rotational E-field is hypothesized to sweep across the neural population and simultaneously activate neurons with different directional sensitivity.

Given the large differences in the volumes of brain where the two TIS E-fields are (approximately) aligned versus not aligned, 1D parameters such as modulation depth, carrier frequency, and envelope do not encompass the full spectrum of TIS scenarios. Capturing the spatial variations in E-field dynamics within individual neurons in

computational simulations requires neuronal models with realistic dendritic and axonal morphology instead of point neuron models (Figure 3A). For a given amplitude ratio of the stimulation channels, only the ratio of the E-field amplitude can be specified for any neuron under the quasi-uniform approximation, whereas no single modulation depth can be defined because the waveform of the E-fields projected along the neural cables varies for different neuronal compartments.

Neuronal response to TIS and other forms of tACS

Stimulation waveforms

Three conventional/quasistatic and three non-quasistatic tACS methods were studied (Figure 2). The conventional methods comprising a single quasistatic E-field include 10 Hz low frequency stimulation (LFS), 2 kHz high frequency stimulation (HFS), and 2 kHz AM-HFS with 10 Hz modulation. Non-quasistatic methods included TIS (two E-fields with 2 kHz and 2.01 kHz frequency, respectively), rotational field HFS (RFS, two E-fields with 2 kHz frequency and a 90° phase shift) and AM-RFS (RFS with 10 Hz-modulated E-fields), which were all simulated with E-field amplitude ratios of 1:1, 2:1, 4:1. The waveforms had a duration of 4 s and, to reduce onset response, 0.5 s and 0.25 s linear ramp-up and ramp-down at the beginning and end, respectively.

Realistic neuron model

To capture fully the effect of TIS, RFS, and AM-RFS on 3D cortical neurons, we used neuron models from the Blue Brain project (Markram et al., 2015; Ramaswamy et al., 2015), which were previously adapted and validated for stimulation with extracellular E-fields (Aberra et al., 2018, 2020). The models were implemented in the NEURON v7.4 (Hines and Carnevale, 1997). Layer 5 (L5) pyramidal cells (PC, Figure 3A) were simulated as they have the largest size and thus lowest thresholds in response to extracellular stimulation (Aberra et al., 2018, 2020). The main axon's terminal was disabled from direct activation to extracellular stimulation to account for the truncation of the main axons in the slicing process and the artificial creation of these low threshold sites (Aberra et al., 2020). To capture the response to kHz stimulation better and match more recent studies of axonal excitability (Engel and Jonas, 2005; Schmidt-Hieber and Bischofberger, 2010), the kinetics of the sodium channels were accelerated by uniformly scaling the time constants of the gating variables of the fast sodium channel (m^3h) by 0.4

for both the opening (*m*) and closing (*h*) gates. The overall effect was a faster firing rate in response to intracellular stimulation, and a decrease in thresholds to kHz stimulation (in the range of −20% to −12.5%) with limited effect on LFS (Figure S1A). We conducted simulations of all stimulation parameters with one representative L5 PC model, and confirmed that the findings are generalizable across cell morphologies with simulations of a subset of parameters in four additional model clones (Figure S2). We also tested the thresholds of a L2/3 PC model and a L4 large basket cell model (data not shown), and did not carry out more extensive characterization of these cell types since their thresholds were significantly higher than those of the L5 PCs for both low and high frequency stimulation.

Simulation setup

The orientations of the E-fields were defined in a spherical coordinate system centered at the neuron's soma and with the polar direction (*z*-axis) aligned with the somatodendritic axis (Figure 3A) (Aberra et al., 2018). Given the alignment of the somatodendritic axis with the cortical column, the polar angle reflects the orientation of the E-field relative to the cortical geometry and more significantly influences activation thresholds, whereas the azimuthal rotation of neuron models within the cortex are random (Aberra et al., 2020). To achieve a uniform representation on the spherical surface, the 32 E-field orientations were taken from a grid of seven non-uniformly sampled polar angles and six uniformly sampled azimuthal angles (Figure 3B). For stimulation methods comprising two E-fields, a total of 1024 orientation combinations were simulated for each parameter setting (i.e., frequency, amplitude modulation, phase shift, and amplitude ratio). NEURON's extracellular mechanism was used for coupling the E-fields to the models. The simulations were set up in MATLAB (versions 2019a and 2020a, The Mathworks, Natick, MA, USA) and performed in NEURON with a time step of 10 μs, which was sufficient to capture the approximately 0.5 ms period of the kHz stimulation and the response of the fast sodium channels with fastest time constant of ~ 40 μs.

The threshold for activation was defined as a response with a firing rate of at least 9.5 Hz at the soma, which is 95% of the 10 Hz frequency of LFS, the difference frequency of TIS, or the frequency of the amplitude modulation (Figure 4A). Bursting was defined as spiking events with less than 15 ms inter-spike intervals within a 50 ms duration (Grossman et al., 2017); if bursting occurred, the bursts were counted instead of individual spikes for

calculating the firing rate in the threshold search. Only spikes within the steady state period of the stimulation were counted, and onset or offset response during the ramp-up and ramp-down time was not considered for threshold determination. Therefore, a suprathreshold response should have at least 31 spikes/bursts during the steady state stimulation period. Setting the threshold firing rate to a slightly lower value allows the neuron's activity to better mimic experimental recordings, in which some trials did not result in firing during every cycle of the LFS or TIS envelope (Grossman et al., 2017). Threshold amplitude was determined by a binary search to 1% accuracy and, for non-quasistatic stimulation methods, was defined as the maximum amplitude of the total E-field.

Thresholds for conduction block (Mirzakhalili et al., 2020) were also obtained to examine whether the non-quasistatic stimulation methods could generate high frequency block similar to conventional kHz currents. Suprathreshold test current pulses were injected into the soma to examine the ability to transmit action potentials. The start of waveforms was therefore delayed by 0.25 s to allow test pulses to be applied during baseline. To further accommodate the strong onset response, the steady state was considered to start 0.25 s after the ramp ended. Therefore, the period for which action potentials were considered for block was 2.75 s, starting 1 s after the stimulus onset. The threshold search was terminated and "no block" was determined for a particular set of stimulation parameters when the maximum tested amplitude of the (first) E-field reached 6000 V/m and action potentials were still occurring during the steady state stimulation period. To match the filtering applied by Grossman et al. (2017) to their patch clamp recordings of cortical and hippocampal neurons, the membrane potential was filtered using a 5th order band stop filter (1 kHz to 15 kHz) and a 3rd order high pass filter (100 Hz). This removes the stimulation "artifact" due to the high stimulation amplitude directly driving the neural membrane above the 0 mV action potential threshold, revealing the underlying action potentials (Figure 4B). Firing patterns were compared for both the raw and filtered membrane potential.

Results

Firing pattern and threshold of activation

We compared the spike timing of model L5 PCs at threshold at several compartments, namely the soma, axon initial segment, first node of the axon (directly connected to the initial segment), and terminal of the main axon. For

all tACS methods and across all E-field orientations or orientation combinations, the spiking events occurred earliest in the first node of the axon. As axon terminals had the lowest thresholds to extracellular stimulation (Aberra et al., 2018; Wang et al., 2018), the responses were all initiated in the axonal arbor and propagated antidromically to the soma and re-orthodromically through the main axon (Aberra et al., 2018, 2020).

At threshold, the firing patterns evoked by all stimulation modalities showed a response before the E-field oscillations reached steady state amplitude (Figure 5), which was not eliminated by the ramp-up of the E-fields. For LFS, AM-HFS, and AM-RFS, the responses during stimulation steady state were single spikes at regular intervals corresponding to the frequency of the stimulation or amplitude modulation, and the early spikes were part of this regular firing. For HFS, TIS, and RFS, the bursts of activity before stimulation reached steady state appeared to be a transient onset response. During steady state stimulation, the HFS and RFS responses consisted of short patterns of two single spikes that repeated regularly but did not satisfy the definition of bursts. The TIS responses exhibited regular firing at the difference frequency for most E-field orientation combinations, and changing the amplitude ratio had negligible effect on the firing pattern. For some orientation combinations, the firing pattern was irregular and contained bursts consisting exclusively of double spikes. For TIS with 1:1 E-field amplitude ratio, bursting occurred in 229 of the 1024 orientation combinations of the E-fields. In orientation combinations where bursts occurred, bursting accounted for 3.2 ± 0.1% of firing events (mean ± standard deviation), whereas among firing events across all orientation combinations, only 0.7% were bursts. Increasing the E-field amplitude ratios to 2:1 and 4:1 reduced the number of orientation combinations evoking bursting and the number of bursts (181, 3.2 ± 0.1%, and 0.6%, and 78, 3.3 ± 0.1%, and 0.2%, respectively). While only TIS evoked bursting at threshold, the neuron model could respond with bursting to suprathreshold stimulation amplitudes for all stimulation modalities (Figure S3).

Activation thresholds were significantly lower for LFS (range 16.9 V/m to 47.4 V/m) compared to all kHz tACS modalities (Figures 6 and S4–S8). The kHz tACS thresholds all fell within a similar range (75 V/m to 230 V/m) despite some variation in their distributions. Thresholds varied with the E-field orientations (Figures S5–S8). Due to the oscillation of the E-fields, the threshold maps were symmetric for points corresponding to E-fields of opposite orientations. The lowest threshold orientation for LFS was aligned with an axon collateral, whereas the lowest

threshold for kHz tACS was aligned with the somatodendritic axis. For TIS, RFS, and AM-RFS, the thresholds increased with the E-field amplitude ratio and showed clustering (Figures 6) for unequal E-field amplitudes due to the dominance of the first E-field.

Firing pattern and threshold of block

At sufficiently high E-field amplitudes, all kHz tACS modalities evoked a strong onset response during ramp up and an offset response during ramp down (Figures 7, 8 and S9). For the majority of E-field orientations of HFS, TIS, and RFS, block could occur during the stimulation steady state for E-field amplitudes (Figures 9 and S10–S14). For all AM-HFS and AM-RFS cases, periodic activation at the frequency of amplitude modulation occurred for all suprathreshold E-field amplitudes. At low stimulation amplitudes, the activation corresponded to the maxima of the AM envelope. At high amplitudes, however, the activation shifted to the minima of the envelope, indicating the activation was an onset/offset response separated by block during periods of high E-field amplitude (Figure S14B and D). Similarly, when sustained block was not observed in TIS, the bursts of firing were shifted by half the modulation period relative to the activation bursting at lower field strengths, and the neural membrane was blocked in between onset/offset responses (Figures 8 and S14C).

Block thresholds had a wide distribution (Figure 9) and were strongly dependent on E-field orientation (Figures S10–S13). Block thresholds for TIS decreased with increasing E-field amplitude ratio, and except for 4:1, were higher compared to HFS and RFS. For TIS with equal E-field amplitudes, neurons were more likely to be exposed to a total E-field with stronger low-frequency modulation (Figure 3A), which generated periodic onset/offset responses interrupting the block. On the other hand, for unequal E-field amplitudes, the modulation was weaker and therefore could achieve block at lower threshold. Block thresholds for RFS increased with amplitude ratio and were similar to HFS. For RFS, equal E-field amplitude exposed more axon terminals to higher aligned E-field at the kHz frequency, resulting in block at lower thresholds. In contrast, some axon terminals were aligned with the weaker E-field of the unequal E-fields, resulting in higher block thresholds.

Discussion

Characteristics of TIS

We quantified the activation and block of model L5 PCs by single channel tACS (10 Hz LFS, 2 kHz HFS, and 10 Hz modulated 2 kHz AM-HFS) as well as methods for modifying the spatial selectivity of tACS using two high-frequency currents to generate E-field temporal interference with two closely spaced frequencies (2 kHz + 2.01 kHz TIS) or E-field rotation through relative phase shift without or with amplitude modulation (2 kHz RFS and 10 Hz modulated 2 kHz AM-RFS). Similar to results reported by Grossman et al. (2017), TIS evoked periodic activation of the model neurons at the difference frequency of the two stimulation currents. Unlike the experimental results, however, TIS thresholds were comparable to those of HFS, as well as those of RFS or their AM versions. In our models, the E-field amplitudes to achieve activation across all forms of kHz tACS ranged from 75 to 230 V/m, which were much higher than the 16.9 to 47.4 V/m range for LFS. At markedly higher stimulation amplitudes (> 1700 V/m), neuronal responses and endogenous activity could be blocked by non-modulated kHz tACS, including TIS. While TIS does generate amplitude modulation of the total E-field projected locally along the neural cables, the magnitude of this modulation is highly dependent on the amplitude ratio of the two E-fields as well as their orientations with respect to the neural cable, and is unlikely to achieve the maximum modulation determined by the E-fields alone. TIS therefore generates block more similarly to regular kHz stimulation than does AM-tACS.

Our study related neuronal responses to the local E-field strength and temporal characteristics. To link the transcranially applied stimulus current with the E-field, Rampersad et al. (2019) simulated the E-field in a mouse brain with a model representing the conditions of the original Grossman et al. (2017) study. They reported TIS E-field maximum of 383 V/m, higher than the threshold E-field values in our study. However, their E-field was defined for the amplitude of the envelope along the orientation of maximum modulation (Grossman et al., 2017; Rampersad et al., 2019)

$$E_{\mathrm{TIS}}^{\mathrm{max.mod.}} = \begin{cases} 2 \cdot \min(|\boldsymbol{E}_1|, |\boldsymbol{E}_2|) & \text{if } |\boldsymbol{E}_1||\sec(\beta)| < |\boldsymbol{E}_2| < |\boldsymbol{E}_1||\cos(\beta)| \\ |(\boldsymbol{E}_1 + \boldsymbol{E}_2) \times (\hat{\boldsymbol{n}}_1 - \hat{\boldsymbol{n}}_2)| & \text{otherwise} \end{cases},$$

where $\beta \in [0, \pi]$ is the angle between the two E-fields and $\hat{\boldsymbol{n}}_{1,2}$ are unit vectors along the E-fields. The E-field along the maximum modulation orientation does not reflect the maximum E-field, $\max|\boldsymbol{E}_{\mathrm{TIS}}(t)|$, over an entire low

frequency period of TIS and, in general, is smaller than the latter (Figure 1B). A metric comparable to our reported thresholds is the maximum E-field amplitude of conventional two-channel tACS with the same combination of E-field orientations and amplitude ratio, which was 38000 V/m (Rampersad et al., 2019, fig. 4B). This value is much higher than our activation thresholds and an order of magnitude higher than the block thresholds. The model by Rampersad et al. did not include the skin, and such high E-field amplitude compared to other studies (Alekseichuk et al., 2019b) may be attributed to the absence of current shunting by conductive soft tissues (Wang et al., 2021b). Nevertheless, even if Rampersad et al. overestimated the E-field by tenfold, our simulation results indicate that TIS applied epicranially to mice could achieve block in cortical neurons, similar to previous computational studies that examined the effects of TIS on peripheral axons (Mirzakhalili et al., 2020). Therefore, the periodic activation observed *in vivo* in mouse experiments may be onset response of nerve block in the target region, in which the block was released periodically due to amplitude modulation of the TIS E-field, whereas the surrounding area was completely blocked due to much smaller modulation. In humans, however, tolerable tACS currents for scalp stimulation without anesthesia are only a few mA and generate E-fields in the brain of only 0.1 V/m to 1 V/m—orders of magnitude lower than both activation and block thresholds of TIS (Huang et al., 2017; Louviot et al., 2022). Our modeling results indicate that suprathreshold TIS would require E-fields in the range from 150 V/m to 800 V/m, corresponding to scalp electrode current of hundreds of mA to over 1 A, which is comparable to or exceeds that in electroconvulsive therapy (Deng et al., 2011; Lee et al., 2015). Therefore, the generation of suprathreshold TIS effects would be intolerable without anesthesia, could result in heating at the electrode–scalp interface, and may induce a seizure with continuous application.

Our results revealed complexities of the E-fields produced by TIS and RFS that have implications for the design and interpretation of modeling and experimental studies. The activation and block thresholds for the E-fields of these non-quasistatic stimulation methods varied not only with their amplitude ratio and angle but also with their orientations relative to the neuron morphology. For example, in the spherical coordinate system used in this study, $\boldsymbol{E}_1$ and $\boldsymbol{E}_2$ with given polar angles ($\theta_{1,2}$) and co-varying azimuths ($\varphi_1 - \varphi_2$ = constant) span a fixed angle, but the thresholds vary significantly (Figure S6–S8 and S12–S13). Therefore, the E-fields obtained along specific directions in computational models, whether for maximum modulation (Huang and Parra, 2019) or in a pre-

determined orientation (Grossman et al., 2017; Rampersad et al., 2019; Song et al., 2021), cannot predict the stimulation effects of TIS, and optimization using E-field simulation alone (Huang et al., 2020; Lee et al., 2022) is unlikely to produce the same results as when considering the effects of the E-field on neurons.

Further, TIS has unique features compared to the other kHz stimulation methods that were tested. TIS creates amplitude modulation in the target region, which is the region where the two E-fields' amplitude are similar. The slight differences of the TIS waveforms for aligned E-field compared to that of a single channel kHz AM-tACS could have non-negligible effects on neural activation. TIS also creates rotational E-field where the two E-field orientations are not directly aligned, which generally coincides with the target region as the two pairs of electrodes are placed on opposite side of the head. In contrast, the E-field of conventional AM-tACS contains no rotation and would only engage a subset of the neural targets recruited by TIS, despite being able to achieve larger modulation depths for a given orientation (Huang and Parra, 2019). The rotation of TIS is emergent due to the varying phase difference during the low frequency cycle, whereas the magnitude of rotation of RFS is sensitive to the phase difference between the waveforms applied at the two pairs of electrodes. In non-target regions, the TIS E-field is mostly oscillatory with minimal rotation and amplitude modulation. This results in similar activation thresholds to HFS and could result in block at high field amplitudes, where higher amplitude ratios would confer lower block thresholds than in the target region. Of the methods capable of producing block, TIS also has the highest block threshold. AM-HFS and AM-RFS cannot achieve block, whereas RFS achieves block at lower thresholds for equal E-field amplitudes compared to unequal amplitudes. On the network level, the asynchronous variation of the TIS E-field over space should be considered (Alekseichuk et al., 2019a). Therefore, experiments such as brain slice studies should consider replicating the features of the TIS E-field with either two stimulation channels or a simultaneously amplitude and frequency modulated E-field, rather than substituting it with a single-frequency AM E-field (Esmaeilpour et al., 2021).

Filtering of membrane potentials

To determine activation thresholds, we analyzed the neuronal responses based on the raw transmembrane potential recordings. At threshold E-field amplitudes, the kHz oscillations of transmembrane potential had limited

amplitudes (5 mV to 15 mV) throughout the cell and did not mask the action potentials. Thus, spike analysis for determination of activation thresholds did not require filtering. For block, the transmembrane potential could be driven beyond 0 mV (or another arbitrarily defined threshold) by kHz waveforms at high amplitudes. These high amplitude oscillations are "real" and not artifacts, making it difficult to distinguish action potentials which ride on top of or are merged with these oscillations. Spikes could nevertheless be identified by temporal or frequency features, as transmembrane potential oscillations of blocked neurons were sinusoidal and removed by filtering, while spikes resulted in distortion that remained after filtering.

In experimental studies of neural stimulation, electrophysiological recordings are contaminated by stimulus artifacts, e.g., the kHz extracellular E-field in TIS. Not only is filtering often necessary as a post-processing step, multiple filters are integral components of the experimental rig before the data are sampled (de Cheveigné and Nelken, 2019). In the study by Grossman et al. (2017), the recorded current clamp traces were band-stop filtered (1 kHz and 15 kHz) and high-pass filtered (100 Hz). While the neurons themselves were unlikely to fire at frequencies over 100 Hz in response to stimulation, it was unclear whether the filtering resulted in the loss of some spikes for the kHz frequency stimulation and TIS. Grossman et al. (2017, fig. S1A–S1I) showed raw recordings and the filtering process, and it appears that spikes could be identified from TIS and HFS only when the artifact amplitude was relatively small and spikes were visible even in the unfiltered traces, i.e., during the initial ramp-up time for both TIS and HFS and during each ramp-up of the low frequency envelope of the TIS waveform. During the steady state of HFS and near the peak of the low frequency envelope of TIS, spikes that were overwhelmed by the artifact could have been lost due to the filtering, leading to a conclusion that there was no response to HFS. As such, alternate artifact removal strategies could be pursued, such as subtraction of an artifact template, or using an ideal notch filter in the frequency domain. Neuronal models are not limited by such artifacts and allow direct access to the transmembrane potential. While advantageous for data analysis, filtering of simulated membrane potentials should be performed with caution as it complicates the interpretation of modeling results and their comparison with experimental studies.

Limitations

Our simulations examined the neuronal response to uniform E-fields under the quasi-uniform approximation for transcranial stimulation. Due to this simplification, the thresholds could not be directly correlated with current amplitudes applied to tACS electrodes, and the spatial distribution of neural activation within the cortex was not determined. Nevertheless, simulations of E-field distributions in realistic head models can easily fill this gap, whether using a multiscale model with neuron models embedded in the cortex (Aberra et al., 2020) or applying the cortical E-field to the uniform field results in our study (Aberra et al., 2022; Bikson et al., 2013). Therefore, the E-field orientation combinations and their amplitude ratios in this study are representative of neurons at different cortical locations.

Despite their realistic morphologies and complexity of ion channels, the model neurons have limitations capturing the response to high frequency stimulation. For extracellular stimulation, axon terminals are the sites of action potential initiation due to their sensitivity to E-fields (Aberra et al., 2018; Wang et al., 2018). However, channel conductances and dynamics are not readily available for the axonal arbor beyond the initial segment and have to be inferred from the parameters of the soma. This may contribute to simulated transcranial stimulation thresholds being on average about two fold higher than experimental data, although the simulated and experimental threshold distributions overlap (Aberra et al., 2020). Further, the sodium ion channel dynamics were fitted to recordings from patch clamp recording (Colbert and Pan, 2002), which could underestimate the kinetics of axonal sodium channels due to filtering (2 kHz low pass filter) and recording below body temperature (24°C). We accelerated the fast sodium channels that contribute the most to action potential firing to capture better the response to kHz stimulation; however, further improvements are required to increase the accuracy of cortical neuron models. Nevertheless, analyses of transcranial stimulation should use cortical neuron models with realistic myelinated axonal morphology at body temperature, and classic Hodgkin-Huxley channels (Cao and Grover, 2019; Xiao et al., 2019) are ill suited to transcranial stimulation studies.

We did not include intrinsic activity or network connectivity in this study. Although the patch clamp recordings in the experiment by Grossman et al. exhibited negligible spontaneous firing in the anesthetized mice (< 0.5 Hz) (2017), intrinsic subthreshold fluctuation of the transmembrane potential could have interacted with the exogenous

E-field. However, threshold changes for stimulation during the afterpolarization of an action potential is on the order of ±50% (McIntyre et al., 2002), and therefore membrane potential fluctuations alone are unlikely to account for the discrepancy of threshold differences between LFS and kHz tACS when comparing the experiments and our simulations. As our goal was to explore the hypothesis of single-neuron demodulation of TIS, we did not include synaptic connections between neurons, and network modulation could be a potential mechanism for TIS. While network activation can be advantageous and exploited to reach deep targets or to improve stimulation efficacy, for example using TMS to modulate the hippocampus, midbrain, or subgenual cingulate by stimulating functionally-connected cortical areas (Luber et al., 2022; Ulrich et al., 2018; Wang et al., 2014; Weigand et al., 2018), it could also be considered a limiting factor on the focality of transcranial stimulation methods, including TIS. For example, Grossman et al. (2017) used c-Fos immunochemistry to demonstrate activation of the hippocampus without activating superficial cortical areas, with strong c-Fos immunoreactivity in the entire region of granule cells within the dentate gyrus. This expression was much stronger than observed anywhere for LFS or elsewhere in TIS, suggesting that TIS achieved strong synchronous activation of the local circuitry in the dentate gyrus, consistent with a seizure-like event evoked by TIS in awake rat (Missey et al., 2021). Furthermore, the area of activation indirectly inferred based on immunohistochemistry does not correlate with the distribution of the simulated E-field modulation envelope amplitude (Grossman et al., 2017, fig. 3, cf. fig. S4), complicating the interpretation of the mechanism and focality of TIS. While these limitations are important directions for future refinement of the models, they would affect similarly TIS and the other forms of kHz stimulation. Therefore, our conclusions regarding the relative effects and thresholds across these modalities appear unlikely to be significantly altered.

Conclusions

We analyzed the E-field characteristics of TIS and quantified the responses of model cortical neurons to TIS and related kHz tACS modalities. The analysis revealed unique spatiotemporal characteristics of the TIS E-field, including phase-shift and frequency jitter of the TIS waveforms due to the difference in E-field amplitudes for aligned E-fields as well as rotation of the total E-field for non-aligned E-fields. These findings highlight the importance of representing the TIS E-field in 3D and using morphologically-realistic neuron models. TIS had

activation thresholds similar to other kHz tACS modalities and much higher than those of low frequency tACS. As expected, the bursts of activation evoked by near-threshold TIS were synchronized with the maxima of the low frequency modulation envelope of the total E-field, providing one possible mechanism for the previously reported experimental responses. Further, at amplitudes exceeding the activation threshold by an order of magnitude, TIS generated neuronal block, and in some cases the modulation of the total E-field caused periodic onset responses, providing an alternative mechanism for the experimental observations. Activation block may also explain the lack of responses in off-target regions, where it can suppress endogenous brain activity. While the neuron models may overestimate absolute activation thresholds, the E-field thresholds for activation and block with TIS are, respectively, two and three orders of magnitude higher than the field strength than can be delivered by tACS with tolerable levels of scalp stimulation. Therefore, administering suprathreshold TIS with transcranial electrical stimulation of the human brain appears infeasible without anesthesia and off-target effects may limit the significance of TIS in general.

Acknowledgment

This work was supported by grants No. R01NS088674 and No. R01NS117405 from the National Institutes of Health of the United States of America; the content is solely the responsibility of the authors and does not necessarily represent the official views of the funding agency or U.S.A. government. Computational support was provided by the Duke Compute Cluster.

The authors thank Dr. Nir Grossman for providing critical feedback on preliminary results at the 2nd Carolina Neuromodulation Conference, Dr. Flavio Fröhlich for discussion on activation mechanism of TIS, Dr. Nicole A Pelot for discussion on onset response of kHz stimulation, Dr. Craig S. Henriquez and Dr. Derek M. Eidum for discussion on rotational E-fields, Dr. Sumientra Rampersad for discussion on E-field simulation in mouse model, and Dr. Huijing Xu, Dr. Gene Yu, and Dr. Alex Goddard for discussion on stimulation of hippocampal neurons.

Author contribution

B. W. developed the theoretical framework, designed the computational study, and performed the neural simulations and data analysis. A. S. A. developed the neuronal models and adjusted ion channel properties. W. M. G. and A.V.P. conceived, supervised, and secured funding and computational resources for the study. B. W. performed data visualization and wrote the manuscript, and all authors revised, commented on, and approved the final version of the manuscript.

Code and data availability statement

The code and data that support the findings of this study are available online at the Research Data Repository (RDR) of Duke University Libraries: https://doi.org/10.7924/r4n87d05r.

Conflict of interest

The authors declare no competing interests.

References

Aberra, A. S., Lopez, A., Grill, W. M., and Peterchev, A. V. *Rapid estimation of cortical neuron activation thresholds by transcranial magnetic stimulation using convolutional neural networks*, pp. 2022.05.18.490331. bioRxiv, 2022.

Aberra, A. S., Peterchev, A. V., and Grill, W. M. Biophysically Realistic Neuron Models for Simulation of Cortical Stimulation. *Journal of Neural Engineering*, 15(6), pp. 066023, 2018.

Aberra, A. S., Wang, B., Grill, W. M., and Peterchev, A. V. Simulation of transcranial magnetic stimulation in head model with morphologically-realistic cortical neurons. *Brain Stimulation*, 13(1), pp. 175–189, 2020.

Alekseichuk, I., Falchier, A. Y., Linn, G., Xu, T., Milham, M. P., Schroeder, C. E., and Opitz, A. Electric field dynamics in the brain during multi-electrode transcranial electric stimulation. *Nature Communications*, 10(1), pp. 2573, 2019a.

Alekseichuk, I., Mantell, K., Shirinpour, S., and Opitz, A. Comparative modeling of transcranial magnetic and electric stimulation in mouse, monkey, and human. *NeuroImage*, 194, pp. 136–148, 2019b.

Barker, A. T., Garnham, C. W., and Freeston, I. L. Magnetic nerve stimulation: the effect of waveform on efficiency, determination of neural membrane time constants and the measurement of stimulator output. *Electroencephalography and Clinical Neurophysiology. Supplement*, 43, pp. 227–237, 1991.

Becker, J. E., Shultz, E. K. B., and Maley, C. T. Transcranial Magnetic Stimulation in Conditions Other than Major Depressive Disorder. *Child and Adolescent Psychiatric Clinics*, 28(1), pp. 45–52, 2019.

Bikson, M., Dmochowski, J., and Rahman, A. The "Quasi-Uniform" Assumption in Animal and Computational Models of Non-Invasive Electrical Stimulation. *Brain Stimulation*, 6(4), pp. 704–705, 2013.

Bossetti, C. A., Birdno, M. J., and Grill, W. M. Analysis of the quasi-static approximation for calculating potentials generated by neural stimulation. *Journal of Neural Engineering*, 5(1), pp. 44–53, 2008.

Cao, J. and Grover, P. STIMULUS: Noninvasive Dynamic Patterns of Neurostimulation Using Spatio-Temporal Interference. *IEEE Transactions on Biomedical Engineering*, 2019.

Caumo, W., Souza, I. C., Torres, I. L., Medeiros, L., Souza, A., Deitos, A., Vidor, L., Fregni, F., and Volz, M. S. Neurobiological Effects of Transcranial Direct Current Stimulation: A Review. *Frontiers in Psychiatry*, 3, 2012.

Colbert, C. M. and Pan, E. Ion channel properties underlying axonal action potential initiation in pyramidal neurons. *Nature Neuroscience*, 5(6), pp. 533, 2002.

Datta, A., Bansal, V., Diaz, J., Patel, J., Reato, D., and Bikson, M. Gyri-precise head model of transcranial direct current stimulation: Improved spatial focality using a ring electrode versus conventional rectangular pad. *Brain Stimulation*, 2(4), pp. 201-207.e1, 2009.

de Cheveigné, A. and Nelken, I. Filters: When, Why, and How (Not) to Use Them. *Neuron*, 102(2), pp. 280–293, 2019.

Deng, Z.-D., Lisanby, S. H., and Peterchev, A. V. Electric field strength and focality in electroconvulsive therapy and magnetic seizure therapy: a finite element simulation study. *Journal of Neural Engineering*, 8(1), pp. 016007, 2011.

Deng, Z.-D., Lisanby, S. H., and Peterchev, A. V. Electric field depth–focality tradeoff in transcranial magnetic stimulation: Simulation comparison of 50 coil designs. *Brain Stimulation*, 6(1), pp. 1–13, 2013.

Dmochowski, J. and Bikson, M. Noninvasive Neuromodulation Goes Deep. *Cell*, 169(6), pp. 977–978, 2017.

Dmochowski, J. P., Datta, A., Bikson, M., Su, Y., and Parra, L. C. Optimized multi-electrode stimulation increases focality and intensity at target. *Journal of Neural Engineering*, 8(4), pp. 046011, 2011.

D'Ostilio, K., Goetz, S. M., Hannah, R., Ciocca, M., Chieffo, R., Chen, J.-C. A., Peterchev, A. V., and Rothwell, J. C. Effect of coil orientation on strength–duration time constant and I-wave activation with controllable pulse parameter transcranial magnetic stimulation. *Clinical Neurophysiology*, 127(1), pp. 675–683, 2016.

Edwards, D., Cortes, M., Datta, A., Minhas, P., Wassermann, E. M., and Bikson, M. Physiological and modeling evidence for focal transcranial electrical brain stimulation in humans: A basis for high-definition tDCS. *NeuroImage*, 74, pp. 266–275, 2013.

Eldaief, M. C., Press, D. Z., and Pascual-Leone, A. Transcranial magnetic stimulation in neurology A review of established and prospective applications. *Neurology: Clinical Practice*, 3(6), pp. 519–526, 2013.

Engel, D. and Jonas, P. Presynaptic Action Potential Amplification by Voltage-Gated Na+ Channels in Hippocampal Mossy Fiber Boutons. *Neuron*, 45(3), pp. 405–417, 2005.

Esmaeilpour, Z., Kronberg, G., Reato, D., Parra, L. C., and Bikson, M. Temporal interference stimulation targets deep brain regions by modulating neural oscillations. *Brain Stimulation*, 14(1), pp. 55–65, 2021.

Goats, G. C. Interferential current therapy. *British Journal of Sports Medicine*, 24(2), pp. 87–92, 1990.

Gomez, L. J., Goetz, S. M., and Peterchev, A. V. Design of transcranial magnetic stimulation coils with optimal trade-off between depth, focality, and energy. *Journal of Neural Engineering*, 15(4), pp. 046033, 2018.

Gomez-Tames, J., Asai, A., and Hirata, A. Multiscale Computational Model Reveals Nerve Response in a Mouse Model for Temporal Interference Brain Stimulation. *Frontiers in Neuroscience*, 15, 2021.

Grossman, N., Bono, D., Dedic, N., Kodandaramaiah, S. B., Rudenko, A., Suk, H.-J., Cassara, A. M., Neufeld, E., Kuster, N., Tsai, L.-H., Pascual-Leone, A., and Boyden, E. S. Noninvasive Deep Brain Stimulation via Temporally Interfering Electric Fields. *Cell*, 169(6), pp. 1029-1041.e16, 2017.

Hines, M. L. and Carnevale, N. T. The NEURON Simulation Environment. *Neural Computation*, 9(6), pp. 1179–1209, 1997.

Howell, B. and McIntyre, C. C. Feasibility of Interferential and Pulsed Transcranial Electrical Stimulation for Neuromodulation at the Human Scale. *Neuromodulation: Technology at the Neural Interface*, n/a(n/a), 2020.

Huang, Y., Datta, A., and Parra, L. C. Optimization of interferential stimulation of the human brain with electrode arrays. *Journal of Neural Engineering*, 17(3), pp. 036023, 2020.

Huang, Y., Liu, A. A., Lafon, B., Friedman, D., Dayan, M., Wang, X., Bikson, M., Doyle, W. K., Devinsky, O., and Parra, L. C. Measurements and models of electric fields in the in vivo human brain during transcranial electric stimulation. *ELife*, 6, pp. e18834, 2017.

Huang, Y. and Parra, L. C. Can transcranial electric stimulation with multiple electrodes reach deep targets? *Brain Stimulation*, 12(1), pp. 30–40, 2019.

Kilgore, K. L. and Bhadra, N. Nerve conduction block utilising high-frequency alternating current. *Medical and Biological Engineering and Computing*, 42(3), pp. 394–406, 2004.

Kloth, L. Interference Current. In *Clinical Electrotherapy*, pp. 183–207. Appleton & Lange, Norwalk Connecticut, 1987.

Lee, S., Lee, C., Park, J., and Im, C.-H. Individually customized transcranial temporal interference stimulation for focused modulation of deep brain structures: a simulation study with different head models. *Scientific Reports*, 10(1), pp. 11730, 2020.

Lee, S., Park, J., Choi, D. S., Lee, C., and Im, C.-H. Multipair transcranial temporal interference stimulation for improved focalized stimulation of deep brain regions: A simulation study. *Computers in Biology and Medicine*, 143, pp. 105337, 2022.

Lee, W. H., Lisanby, S. H., Laine, A. F., and Peterchev, A. V. Electric Field Model of Transcranial Electric Stimulation in Nonhuman Primates: Correspondence to Individual Motor Threshold. *IEEE Transactions on Biomedical Engineering*, 62(9), pp. 2095–2105, 2015.

Lefaucheur, J.-P., André-Obadia, N., Antal, A., Ayache, S. S., Baeken, C., Benninger, D. H., Cantello, R. M., Cincotta, M., de Carvalho, M., De Ridder, D., Devanne, H., Di Lazzaro, V., Filipović, S. R., Hummel, F. C., Jääskeläinen, S. K., Kimiskidis, V. K., Koch, G., Langguth, B., Nyffeler, T., Oliviero, A., Padberg, F., Poulet, E., Rossi, S., Rossini, P. M., Rothwell, J. C., Schönfeldt-Lecuona, C., Siebner, H. R., Slotema, C. W., Stagg, C. J., Valls-Sole, J., Ziemann, U., Paulus, W., and Garcia-Larrea, L. Evidence-based guidelines on the therapeutic use of repetitive transcranial magnetic stimulation (rTMS). *Clinical Neurophysiology*, 125(11), pp. 2150–2206, 2014.

Louviot, S., Tyvaert, L., Maillard, L. G., Colnat-Coulbois, S., Dmochowski, J., and Koessler, L. Transcranial Electrical Stimulation generates electric fields in deep human brain structures. *Brain Stimulation*, 15(1), pp. 1–12, 2022.

Luber, B., Davis, S. W., Deng, Z.-D., Murphy, D., Martella, A., Peterchev, A. V., and Lisanby, S. H. Using diffusion tensor imaging to effectively target TMS to deep brain structures. *NeuroImage*, 249, pp. 118863, 2022.

Markram, H., Muller, E., Ramaswamy, S., Reimann, M. W., Abdellah, M., Sanchez, C. A., Ailamaki, A., Alonso-Nanclares, L., Antille, N., Arsever, S., Kahou, G. A. A., Berger, T. K., Bilgili, A., Buncic, N., Chalimourda, A., Chindemi, G., Courcol, J.-D., Delalondre, F., Delattre, V., Druckmann, S., Dumusc, R., Dynes, J., Eilemann, S., Gal, E., Gevaert, M. E., Ghobril, J.-P., Gidon, A., Graham, J. W., Gupta, A., Haenel, V., Hay, E., Heinis, T., Hernando, J. B., Hines, M., Kanari, L., Keller, D., Kenyon, J., Khazen, G., Kim, Y., King, J. G., Kisvarday, Z., Kumbhar, P., Lasserre, S., Le Bé, J.-V., Magalhães, B. R. C., Merchán-Pérez, A., Meystre, J., Morrice, B. R., Muller, J., Muñoz-Céspedes, A., Muralidhar, S., Muthurasa, K., Nachbaur, D., Newton, T. H., Nolte, M., Ovcharenko, A., Palacios, J., Pastor, L., Perin, R., Ranjan, R., Riachi, I., Rodríguez, J.-R., Riquelme, J. L., Rössert, C., Sfyrakis, K., Shi, Y., Shillcock, J. C., Silberberg, G., Silva, R., Tauheed, F., Telefont, M., Toledo-Rodriguez, M., Tränkler, T., Van Geit, W., Díaz, J. V., Walker, R.,

Wang, Y., Zaninetta, S. M., DeFelipe, J., Hill, S. L., Segev, I., and Schürmann, F. Reconstruction and Simulation of Neocortical Microcircuitry. *Cell*, 163(2), pp. 456–492, 2015.

McIntyre, C. C., Richardson, A. G., and Grill, W. M. Modeling the Excitability of Mammalian Nerve Fibers: Influence of Afterpotentials on the Recovery Cycle. *Journal of Neurophysiology*, 87(2), pp. 995–1006, 2002.

Miles, J. D., Kilgore, K. L., Bhadra, N., and Lahowetz, E. A. Effects of ramped amplitude waveforms on the onset response of high-frequency mammalian nerve block. *Journal of Neural Engineering*, 4(4), pp. 390, 2007.

Miranda, P. C., Mekonnen, A., Salvador, R., and Ruffini, G. The electric field in the cortex during transcranial current stimulation. *NeuroImage*, 70, pp. 48–58, 2013.

Mirzakhalili, E., Barra, B., Capogrosso, M., and Lempka, S. F. Biophysics of Temporal Interference Stimulation. *Cell Systems*, 11(6), pp. 557-572.e5, 2020.

Missey, F., Rusina, E., Acerbo, E., Botzanowski, B., Trébuchon, A., Bartolomei, F., Jirsa, V., Carron, R., and Williamson, A. Orientation of Temporal Interference for Non-invasive Deep Brain Stimulation in Epilepsy. *Frontiers in Neuroscience*, 15, 2021.

Pelot, N. A., Behrend, C. E., and Grill, W. M. Modeling the response of small myelinated axons in a compound nerve to kilohertz frequency signals. *Journal of Neural Engineering*, 14(4), pp. 046022, 2017.

Peterchev, A. V., Goetz, S. M., Westin, G. G., Luber, B., and Lisanby, S. H. Pulse width dependence of motor threshold and input–output curve characterized with controllable pulse parameter transcranial magnetic stimulation. *Clinical Neurophysiology*, 124(7), pp. 1364–1372, 2013.

Plonsey, R. and Heppner, D. B. Considerations of quasi-stationarity in electrophysiological systems. *The Bulletin of Mathematical Biophysics*, 29(4), pp. 657–664, 1967.

Ramaswamy, S., Courcol, J.-D., Abdellah, M., Adaszewski, S. R., Antille, N., Arsever, S., Atenekeng, G., Bilgili, A., Brukau, Y., Chalimourda, A., Chindemi, G., Delalondre, F., Dumusc, R., Eilemann, S., Gevaert, M. E., Gleeson, P., Graham, J. W., Hernando, J. B., Kanari, L., Katkov, Y., Keller, D., King, J. G., Ranjan, R., Reimann, M. W., Rössert, C., Shi, Y., Shillcock, J. C., Telefont, M., Van Geit, W., Villafranca Diaz, J., Walker, R., Wang, Y., Zaninetta, S. M., DeFelipe, J., Hill, S. L., Muller, J., Segev, I., Schürmann, F., Muller, E. B., and Markram, H. The neocortical microcircuit collaboration portal: a resource for rat somatosensory cortex. *Frontiers in Neural Circuits*, 9, 2015.

Rampersad, S., Roig-Solvas, B., Yarossi, M., Kulkarni, P. P., Santarnecchi, E., Dorval, A. D., and Brooks, D. H. Prospects for transcranial temporal interference stimulation in humans: A computational study. *NeuroImage*, 202, pp. 116124, 2019.

Reato, D., Rahman, A., Bikson, M., and Parra, L. C. Effects of weak transcranial alternating current stimulation on brain activity—a review of known mechanisms from animal studies. *Frontiers in Human Neuroscience*, 7, pp. 687, 2013.

Rossi, S., Antal, A., Bestmann, S., Bikson, M., Brewer, C., Brockmöller, J., Carpenter, L. L., Cincotta, M., Chen, R., Daskalakis, J. D., Di Lazzaro, V., Fox, M. D., George, M. S., Gilbert, D., Kimiskidis, V. K., Koch, G., Ilmoniemi, R. J., Pascal Lefaucheur, J., Leocani, L., Lisanby, S. H., Miniussi, C., Padberg, F., Pascual-Leone, A., Paulus, W., Peterchev, A. V., Quartarone, A., Rotenberg, A., Rothwell, J., Rossini, P. M., Santarnecchi, E., Shafi, M. M., Siebner, H. R., Ugawa, Y., Wassermann, E. M., Zangen, A., Ziemann, U.,

and Hallett, M. Safety and recommendations for TMS use in healthy subjects and patient populations, with updates on training, ethical and regulatory issues: Expert Guidelines. *Clinical Neurophysiology*, 2020.

Rotem, A., Neef, A., Neef, N. E., Agudelo-Toro, A., Rakhmilevitch, D., Paulus, W., and Moses, E. Solving the Orientation Specific Constraints in Transcranial Magnetic Stimulation by Rotating Fields. *PLOS ONE*, 9(2), pp. e86794, 2014.

Roth, Y., Pell, G., Ankry, M., Hadad, Y., Eisen, A., Burnishev, Y., Tendler, A., Moses, E., and Zangen, A. Comparing rotational-field-dTMS to unidirectional-dTMS in healthy volunteers. *Brain Stimulation*, 12(2), pp. 390, 2019.

Roth, Y., Pell, G. S., Barnea-Ygael, N., Ankry, M., Hadad, Y., Eisen, A., Burnishev, Y., Tendler, A., Moses, E., and Zangen, A. Rotational field TMS: Comparison with conventional TMS based on motor evoked potentials and thresholds in the hand and leg motor cortices. *Brain Stimulation*, 13(3), pp. 900–907, 2020.

Schmidt-Hieber, C. and Bischofberger, J. Fast Sodium Channel Gating Supports Localized and Efficient Axonal Action Potential Initiation. *Journal of Neuroscience*, 30(30), pp. 10233–10242, 2010.

Song, X., Zhao, X., Li, X., Liu, S., and Ming, D. Multi-channel transcranial temporally interfering stimulation (tTIS): application to living mice brain. *Journal of Neural Engineering*, 18(3), pp. 036003, 2021.

Sorkhabi, M. M., Wendt, K., and Denison, T. Temporally Interfering TMS: Focal and Dynamic Stimulation Location. In *2020 42nd Annual International Conference of the IEEE Engineering in Medicine Biology Society (EMBC)*, pp. 3537–3543, 2020.

Ulrich, M., Lorenz, S., Spitzer, M. W., Steigleder, L., Kammer, T., and Grön, G. Theta-burst modulation of mid-ventrolateral prefrontal cortex affects salience coding in the human ventral tegmental area. *Appetite*, 123, pp. 91–100, 2018.

Vöröslakos, M., Takeuchi, Y., Brinyiczki, K., Zombori, T., Oliva, A., Fernández-Ruiz, A., Kozák, G., Kincses, Z. T., Iványi, B., Buzsáki, G., and Berényi, A. Direct effects of transcranial electric stimulation on brain circuits in rats and humans. *Nature Communications*, 9(1), pp. 483, 2018.

Wang, B., Aberra, A., Grill, W., and Peterchev, A. Comparing temporal interference stimulation and other kilohertz stimulation modalities using computational models. *Brain Stimulation*, 14(6), pp. 1679, 2021a.

Wang, B., Aberra, A. S., Grill, W. M., and Peterchev, A. V. Modified cable equation incorporating transverse polarization of neuronal membranes for accurate coupling of electric fields. *Journal of Neural Engineering*, 15(2), pp. 026003, 2018.

Wang, B., Aberra, A. S., Grill, W. M., and Peterchev, A. V. Physics and Biophysics Fundamentals of Transcranial Stimulation. In *The Oxford Handbook of Transcranial Stimulation*, 2nd ed., pp. 23. Oxford University Press, Oxford, 2021b.

Wang, J. X., Rogers, L. M., Gross, E. Z., Ryals, A. J., Dokucu, M. E., Brandstatt, K. L., Hermiller, M. S., and Voss, J. L. Targeted enhancement of cortical-hippocampal brain networks and associative memory. *Science*, 345(6200), pp. 1054–1057, 2014.

Weigand, A., Horn, A., Caballero, R., Cooke, D., Stern, A. P., Taylor, S. F., Press, D., Pascual-Leone, A., and Fox, M. D. Prospective Validation That Subgenual Connectivity Predicts Antidepressant Efficacy of Transcranial Magnetic Stimulation Sites. *Biological Psychiatry*, 84(1), pp. 28–37, 2018.

Xiao, Q., Zhong, Z., Lai, X., and Qin, H. A multiple modulation synthesis method with high spatial resolution for noninvasive neurostimulation. *PLOS ONE*, 14(6), pp. e0218293, 2019.

Figures

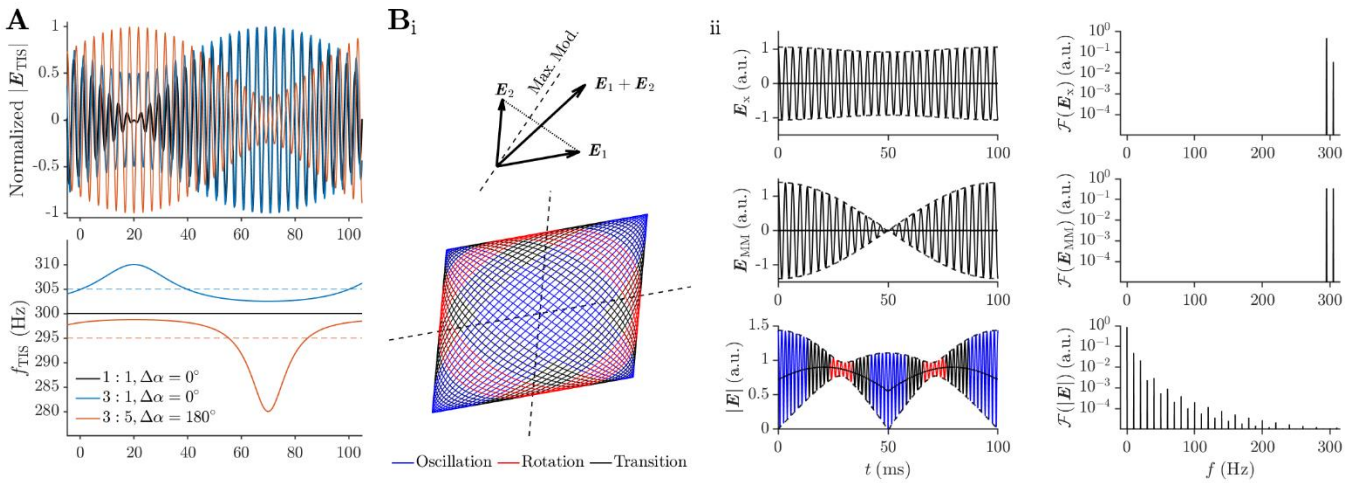

Figure 1. Time and frequency domain characteristics of TIS E-fields

A. Characteristic of two aligned or anti-aligned E-fields. The channels have relatively low frequencies (295 Hz and 305 Hz) for better visualization. Top: for aligned E-fields (blue and black), the high frequency oscillations of the total E-fields (normalized) are in-phase only at the peaks of their envelopes and shift out of phase at the troughs. For anti-aligned fields (orange), the envelopes themselves are 180° out-of-phase compared to the those of aligned E-fields (blue or black), whereas the carrier could be in-phase at a peak/trough (red and blue, in-phase at $t \approx 120$ ms) or in between peak and trough (red and black, in-phase at $t \approx 40$ ms). Bottom: the carrier frequency of the total E-field includes a low frequency jitter around the frequency of the E-field with larger amplitude. **B.** Characteristic of two non-aligned E-fields with an amplitude ratio of 5:4 and a 75° angle. **i.** Top: the two E-fields of TIS span a plane containing the direction of maximum modulation (Max. Mod., dashed line). Bottom: the end point of the total E-field vector traces out a Lissajous curve, which alternates between oscillatory (blue) and rotational (red) periods. Here, oscillation and rotation are (arbitrarily) defined as the E-field magnitude having a ratio of minimum versus maximum smaller than 1/3 or larger than 2/3 during one high frequency cycle, respectively. **ii.** The total E-field projected along any direction, for example the x-axis ($\boldsymbol{E}_x$, top row) or the direction of maximum modulation ($\boldsymbol{E}_{\mathrm{MM}}$, middle row), has a low frequency envelope (left column, dashed lines) but the oscillations average out to zero (thick line) and therefore the waveform does not contain low frequency energy in the spectrum (right column). The E-

field magnitude (bottom row) has low frequency content, and the oscillatory periods could be a driving factor of TIS. $\mathcal{F}$: Fourier transform. a.u.: arbitrary units.

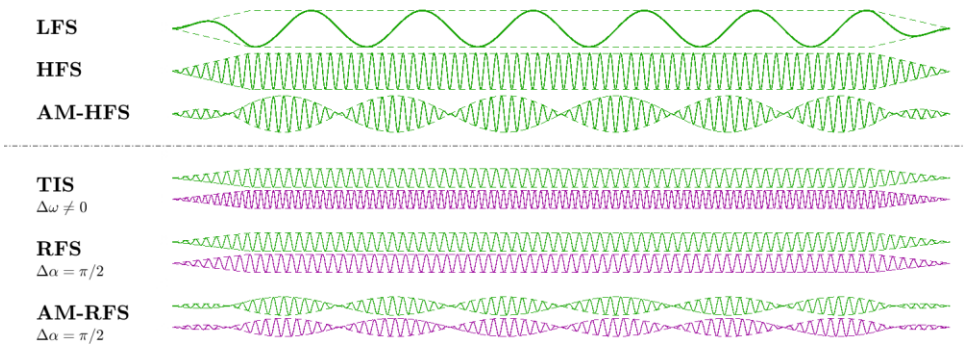

Figure 2. Current waveforms of various tACS modalities

Illustration of the waveforms of low frequency stimulation (LFS), high frequency stimulation (HFS), amplitude-modulated HFS (AM-HFS), temporal interference stimulation (TIS), rotational field HFS (RFS), and amplitude-modulated RFS (AM-RFS). The waveforms of the conventional methods and the first E-field of non-quasistatic stimulation methods are shown in green, and the waveform of the second E-field of non-quasistatic stimulation methods are shown in purple. The envelope of all waveforms is shown with dashed lines and has a ramp-up and ramp-down period. The relative frequencies are for visualization and not to scale with the actual stimulation methods.

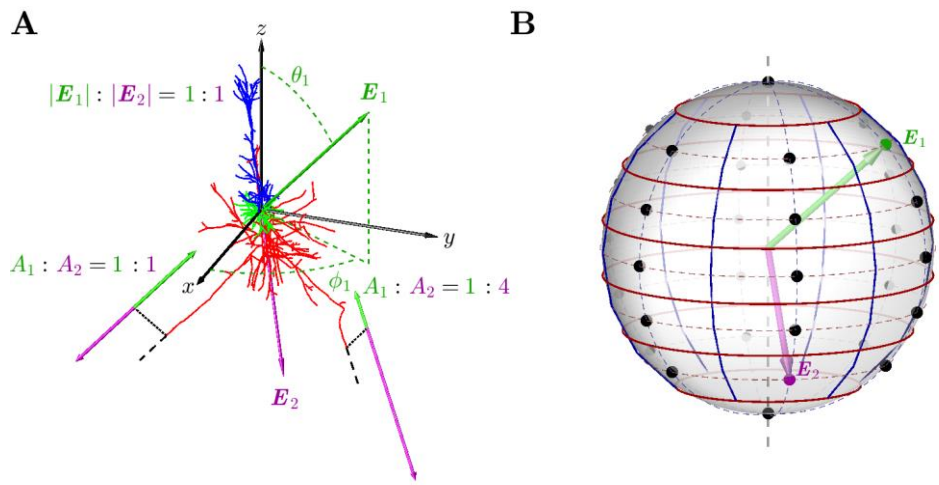

Figure 3. Neuron model and definitions of E-field orientation

A. L5 PC morphology and the spherical coordinate system for E-field orientation. The origin is located at the soma with the *z*-axis aligned along the somatodendritic axis. The E-fields are defined by their polar and azimuthal angles, θ and ϕ, shown for the first E-field (green) as example. The E-fields have different effective amplitudes (A_1, A_2) at different locations along the neural cable, as shown at two terminals in the axonal arbor, with the black dashed lines showing the orientation of the axon at the terminals. Color legend for neuron: apical dendrite in blue, basal dendrite in green, and axon in red. **B.** Sampling of 32 E-field orientations for the 3D neuron model as represented by dots on a spherical surface, with black and grey dots indicating the front and back of the sphere. The polar axis is shown as a vertical dashed line.

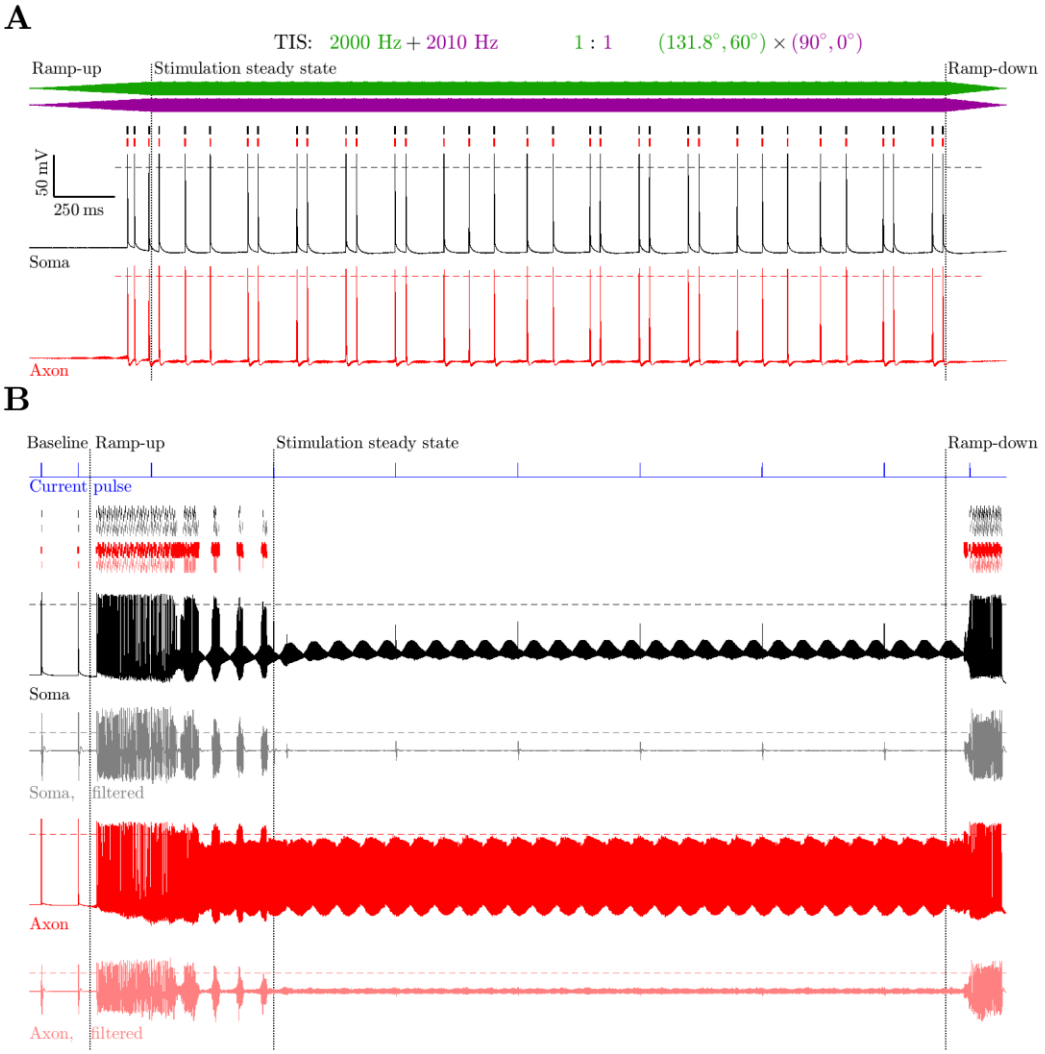

Figure 4. Neural response and neural recording processing

A. Example response of L5 PC firing in response to TIS at threshold. The stimulation waveforms of the two E-fields are shown on top, followed by the raster plots of firing and the membrane potentials for the soma (black) and an axon node (red). Individual spikes or the first spike within a burst are aligned horizontally, with additional spikes within a burst offset vertically. The dotted vertical lines mark the start and end of the stimulation steady state period between 0.75 s and 3.75 s, and the horizontal dashed line mark the spike thresholds. **B.** Example response of L5 PC conduction block in response to TIS at high stimulation amplitude. Suprathreshold intracellular current pulses (blue) were applied to the soma and evoked action potentials at baseline. However, they did not evoke action potentials in the stimulation steady state, either in the raw (black) or filtered (grey) membrane potential. The membrane potential

deflection in the soma generated by the test current pulse did not generate action potential in the axon (red traces). The dotted vertical lines mark the baseline period ending at 0.25 s and start and end of the stimulation's steady state period between 1 s and 3.75 s.

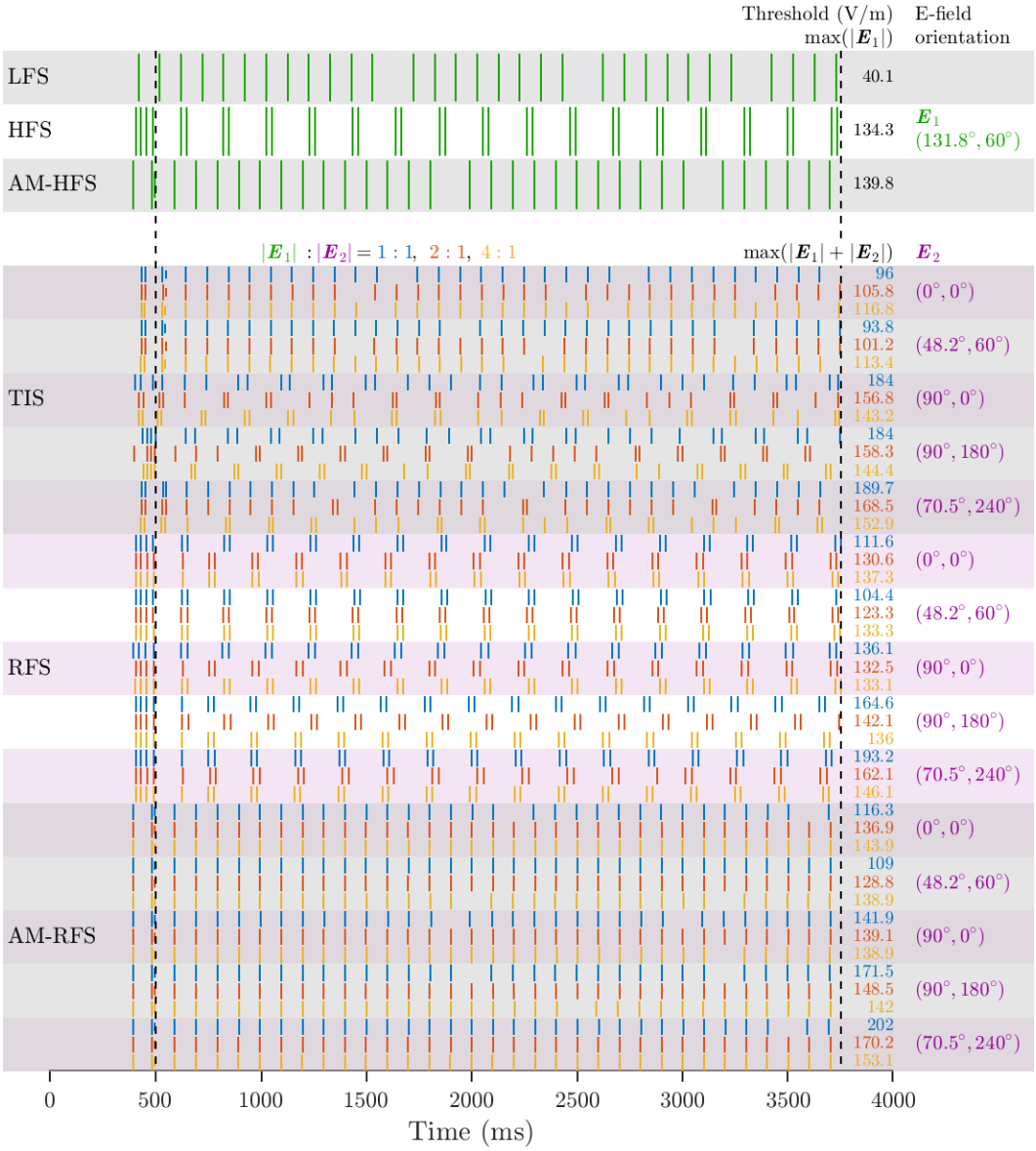

Figure 5. Representative responses of L5 PC at activation threshold

Raster plot of somatic firing. The same orientation is chosen for the E-field of LFS, HFS, and AM-HFS as well as the first E-field of TIS, RFS, and AM-RFS. The same five orientations are chosen for the second E-field of TIS, RFS, and AM-RFS, with results for all 3 amplitude ratios of the two E-fields shown (from top to bottom: 1:1, 2:1, 4:1 in blue, red, and yellow, respectively). The dotted vertical lines mark the start and end of the stimulation steady state period between 0.5 s and 3.75 s.

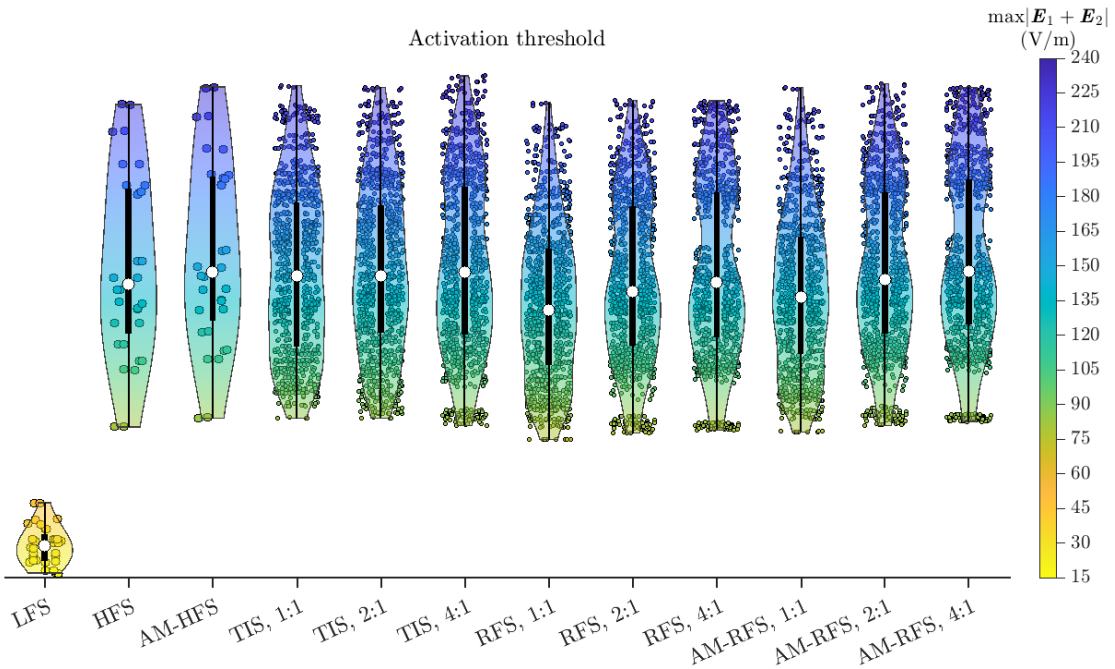

Figure 6. Activation threshold

Thresholds for action potential generation for all 32 orientations (LFS, HFS, and AM-HFS) and 1024 orientation combinations (TIS, RFS, and AM-RFS) of E-field(s). Each violin plot shows the individual data points as circles (with jitter fixed for the E-field orientations and orientation combinations), the estimated density of distribution as a shaded area, the white circle representing median, thick bar covering first to third quartiles, and thin line extending 1.5 times the interquartile range above and below the quartiles.

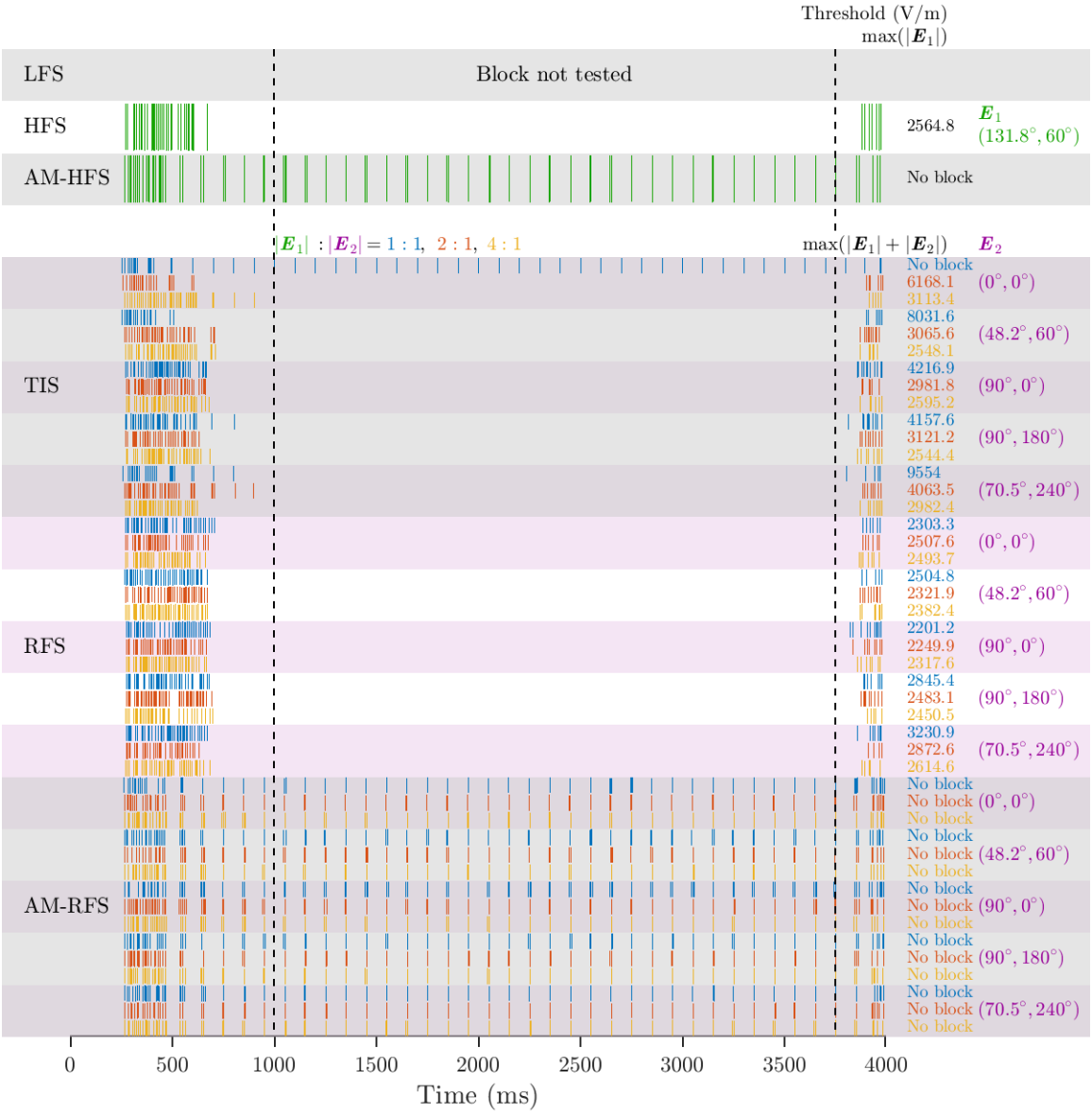

Figure 7. Representative responses of L5 PC at block thresholds or maximum amplitude tested

Raster plot of somatic firing for the same E-field orientations as in Figure 5, showing the spikes of the filtered transmembrane potential of the soma. Same results for spikes of the raw transmembrane potential are shown in Fig. S8.

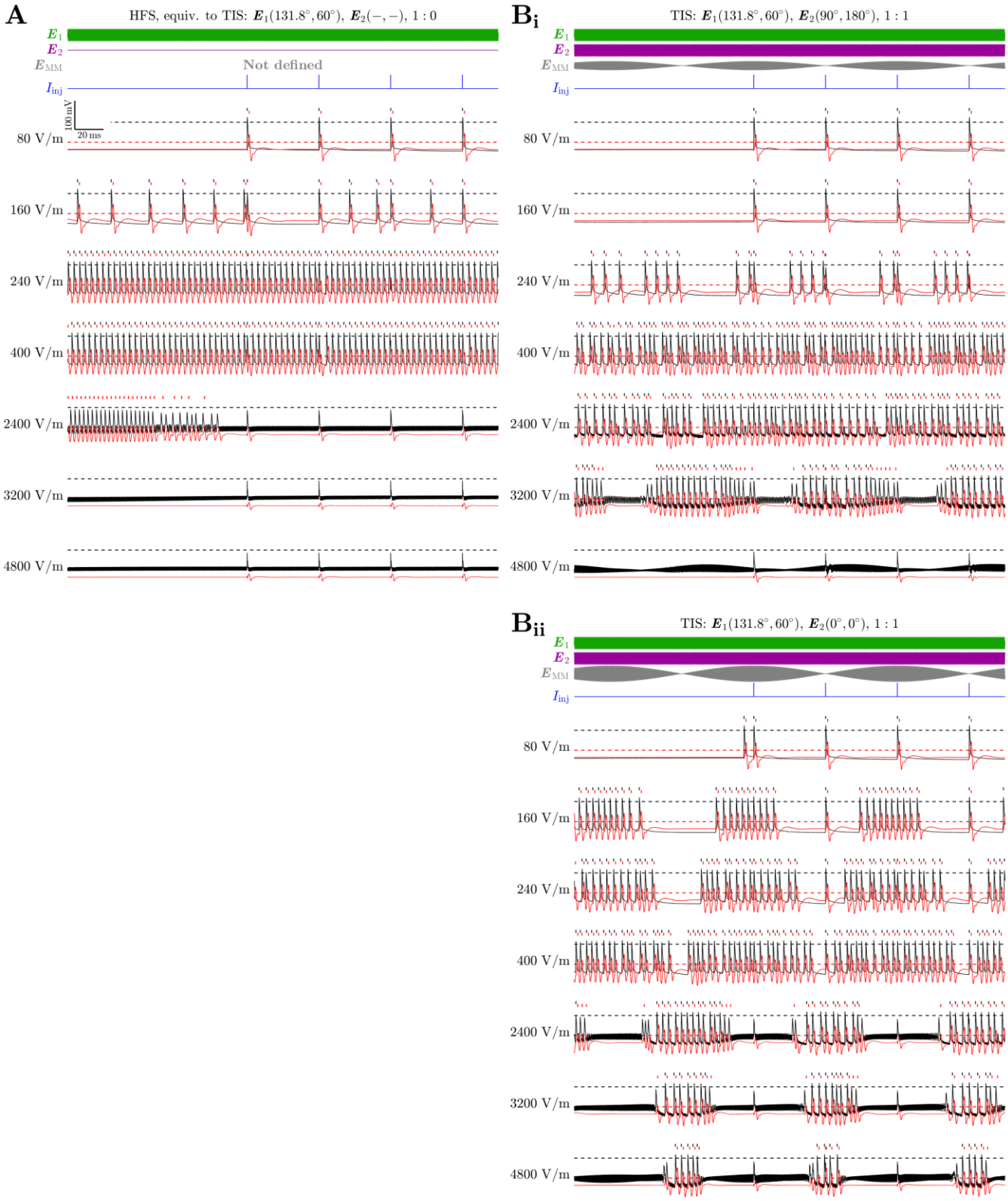
A
HFS, equiv. to TIS: $\boldsymbol{E}_1(131.8°, 60°)$, $\boldsymbol{E}_2(-,-)$, 1 : 0
$\boldsymbol{E}_1$
$\boldsymbol{E}_2$
E_{MM}
Not defined
I_{inj}
100 mV
20 ms
80 V/m
160 V/m
240 V/m
400 V/m
2400 V/m
3200 V/m
4800 V/m
$\mathbf{B_i}$
TIS: $\boldsymbol{E}_1(131.8°, 60°)$, $\boldsymbol{E}_2(90°, 180°)$, 1 : 1
$\mathbf{B_{ii}}$
TIS: $\boldsymbol{E}_1(131.8°, 60°)$, $\boldsymbol{E}_2(0°, 0°)$, 1 : 1

Figure 8. Representative neuron firing evoked by HFS and TIS for a range of E-field amplitudes

The raw (black) and filtered (red, filter parameters defined in *Simulation setup* subsection) transmembrane potential at the soma with action potential timing marked with vertical lines for seven different E-field amplitudes given on the left as either max($|\boldsymbol{E}_1|$) for HFS or max($|\boldsymbol{E}_1+\boldsymbol{E}_2|$) for TIS. The dashed lines shows the action potential threshold of 25 mV for both raw and filtered transmembrane potentials. Shown on top are the individual E-field waveforms (green and purple), total E-field along the direction of maximum modulation ($\boldsymbol{E}_{\mathrm{MM}}$, gray), and timing of suprathreshold current injection test pulse (I_{inj}, blue). The orientation of the (first) E-field is the same as in Figures 5 and 7, and two of the orientations of the second E-field are shown. **A.** HFS, which is equivalent to TIS with 1:0 field amplitude ratio, evokes sustained firing with increased E-field amplitude and results in block for high stimulation amplitude. **B.** TIS exhibits periodic firing at lower amplitudes, which becomes sustained firing similar to HFS at higher amplitude, and then becomes periodic again at even higher amplitudes as the amplitude modulation of the total TIS E-field results in onset/offset firing. Depending on the E-field orientations and corresponding amplitude modulation of the total E-field, the onset/offset firing may cease (**B$_{\mathbf{i}}$**) or persist (**B$_{\mathbf{ii}}$**) at higher E-field amplitude, but the transmembrane potential reaches a blocked state that does not respond to stimulation.

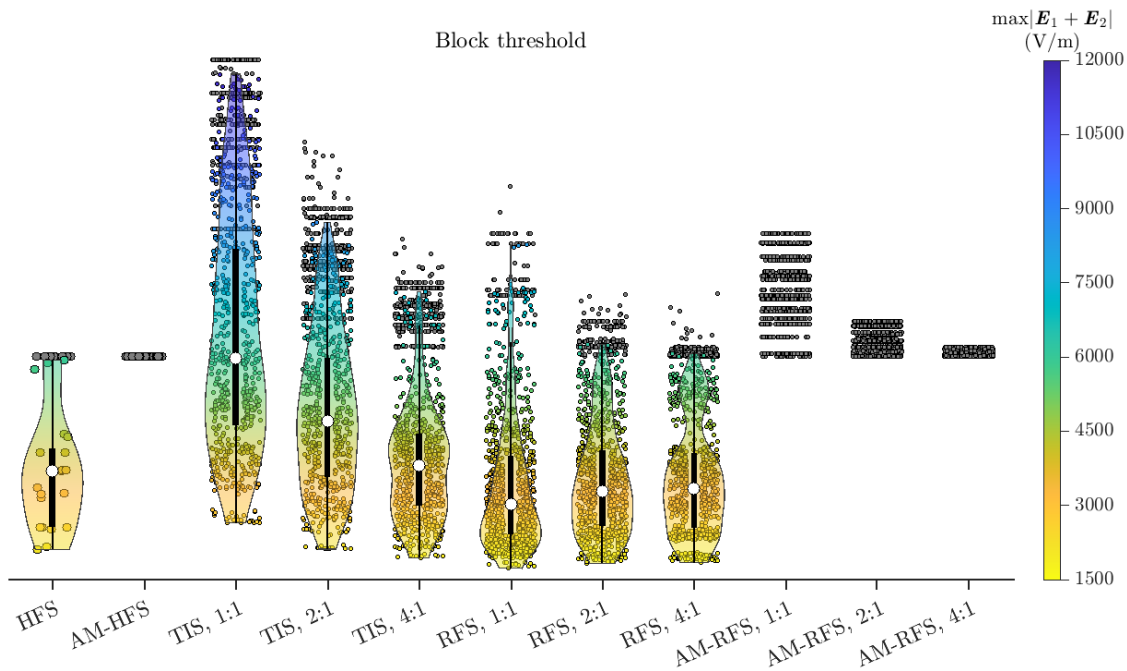

Figure 9. Block threshold

Thresholds for all 32 orientations (HFS and AM-HFS) and 1024 orientation combinations (TIS, RFS, and AM-RFS) of E-field, in a format similar to Figure 6. Orientation (combination) that could not achieve block with $|\boldsymbol{E}_1| \leq 6000$ V/m are shown as grey circles.